Reentrant Rigidity Transition in Planar Epithelia with Volume and Area Elasticity

Tanmoy Sarkar[1,2] and Matej Krajnc[1,*]
[1]Jožef Stefan Institute, Jamova 39, SI-1000 Ljubljana, Slovenia
[2]School of Physics, Indian Institute of Science Education and Research Thiruvananthapuram, Maruthamala PO, Thiruvananthapuram, Kerala 695551, India

(Received 20 May 2025; accepted 22 January 2026; published 12 February 2026)

We find a reentrant columnar-to-squamous rigidity transition in three-dimensional (3D) epithelia, governed by volume and area elasticity. Our model maps to the classic 2D area- and perimeter-elasticity model but, unlike its 2D counterpart, shows compression-induced softening or stiffening, depending on the initial state. The phase diagram reveals floppy states with vanishing shear and in-plane bulk moduli, alongside a lateral-tension-driven discontinuous columnar-to-squamous transition. The critical behavior underlying the emergence of the reentrant transition belongs to the mean-field universality class.

DOI: 10.1103/ky2j-5nwx

Introduction—During morphogenesis, epithelial tissues must have an ability to transition dynamically between elastic and fluidlike states to support mechanical stresses on one hand and facilitate cellular rearrangements and large-scale tissue flows on the other [1–7]. This dual solid-fluid behavior has been widely studied using the two-dimensional (2D) area- and perimeter-elasticity (APE) model, which assumes that each cell's apical area A and perimeter P tend toward preferred values A_0 and P_0, respectively [8–12]. The model predicts a rigidity transition controlled by the preferred cell shape: Tissues are rigid when the actual cell shapes are incompatible with the preferred one and floppy when cells can attain their preferred areas and perimeters [13,14]. In the floppy regime, the linear shear modulus vanishes and, depending on their structure, tissues may also display zero energy barriers for cell rearrangements [11,15].

These findings extend to fully three-dimensional (3D) space-filling cell aggregates [16]. Analogous to 2D, the generalized 3D model employs volume and area elasticity (VAE), minimizing the energy when cell volumes and surface areas match the preferred values V_0 and S_0, respectively. As in 2D, the preferred 3D cell shape controls rigidity and the linear shear modulus vanishes when tissues transition from rigid to floppy states [16].

Generalizing the 2D APE model to 3D epithelial monolayers has proven more subtle. A natural approach is to couple the APE framework—capturing the mechanics of apically positioned adherens junctions and actomyosin cortices—to the basolateral cell surfaces under surface tension. Yet this apico-basolateral coupling suppresses the rigidity transition, rendering tissues rigid regardless of the preferred apical cell shape [17]. This raises the central question of our Letter: Do the physics underlying the 2D APE model carry over to 3D monolayers? More specifically, what theoretical framework can account for a rigidity transition in 3D monolayers in a way that remains consistent with the 2D APE model?

Here, we address these questions by studying the mechanics of 3D monolayers governed by VAE. By 2D projecting our model, we explore its relation to the APE model and confirm that the properties of epithelia, studied in 2D, are generally translatable to 3D. We characterize, both analytically and numerically, the phase diagram of rigid and floppy monolayers and find a novel reentrant rigidity transition, controlled by in-plane isotropic strain. The model also features a regime of floppy states with a vanishing 2D bulk modulus, associated with isotropic in-plane deformations, and a discontinuous columnar-to-squamous transition (CST), controlled by cell-cell adhesion. Importantly, our Letter shows that 3D cell shapes fundamentally affect tissue's response to isotropic compression. While the 2D model, counterintuitively, predicts tissue softening upon compression and stiffening upon dilation [18,19], tissues in our 3D model are rigidified both when compressed and dilated.

The model—We consider ordered and disordered planar packings of $N_c = 1024$ prismatic cells with periodic boundary conditions, assuming uniform cell height across the tissue (Fig. 1 and [20]). In addition to VAE that penalizes deviations of cell volumes V_k and cell surface areas S_k from preferred values, our potential energy includes a constant contribution to the lateral surface tension $-\gamma$, describing cell-cell adhesion at the lateral cell sides; we denote the lateral cell surface areas by $A_k^{(l)}$ and,

*Contact author: matej.krajnc@ijs.si

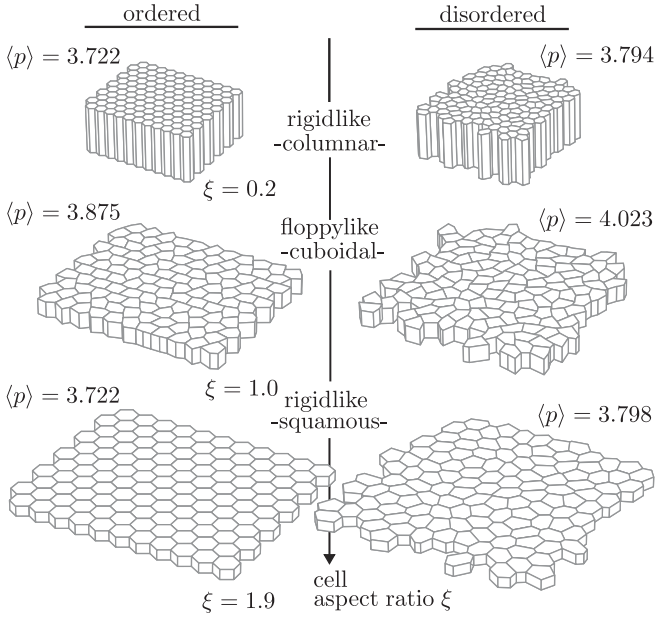

FIG. 1. Simulation snapshots of CST. Ordered (left) and disordered (right) tissues for $S_0 = 5.75$ and 5.9, respectively, and $\gamma = 0.5$. For clarity, ~10% of all cells are shown. The fraction of nonhexagons in disordered sample $d = 0.437$ [21].

for generality, we consider both positive and negative γ values. In dimensionless form, where units of energy and length are given by $k_S V_0^{4/3}$ (k_S being the area-elasticity modulus) and $V_0^{1/3}$, respectively, the potential energy reads

$$W = \sum_k \left[k_V (V_k - 1)^2 + (S_k - S_0)^2 - \frac{\gamma}{2} A_k^{(l)} \right]. \quad (1)$$

Here k_V is a dimensionless cell-incompressibility modulus; for simplicity, we begin by treating cells as nearly incompressible, i.e., $k_V = 100$, and we show in Supplemental Material, Sec. IV [21] that finite k_V does not fundamentally affect the main conclusions of our Letter. Details related to the implementation of the vertex model and statistical properties of disordered cell packings are given in Supplemental Material, Secs. I and II and Fig. S1 [21].

We simulate CST in both ordered and disordered cell monolayers by quasistatically and isotropically increasing the simulation-box size (Fig. 1). Because of cell incompressibility, the in-plane area increase implies an increase of the 3D cell aspect ratio (i.e., width-to-height ratio), defined as

$$\xi = \frac{\sqrt{A}}{h} \overset{V=1}{=} A^{3/2}, \quad (2)$$

where A and $h = A^{-1}$ are the in-plane cell area and height, respectively. Our simulations assume apicobasal symmetry in cell shapes, however, even in the absence of this constraint, cell shapes *are* apicobasally symmetric, consistent with the inherent apicobasal symmetry of the mechanics [Eq. (1)]. The exception are highly columnar disordered tissues, where cells with pentagonal bases become either apically or basally constricted [25,26]. Importantly, this instability [27] does not break the global apicobasal symmetry of the tissue, in contrast to the asymmetry observed in the model by Rozman *et al.* [17].

We measure average in-plane cell-shape indices, defined as $\langle p \rangle = \langle P_k / \sqrt{A} \rangle$, where P_k is the cell in-plane perimeter, and find that $\langle p \rangle$ nonmonotonically depends on ξ, such that the in-plane structure of columnar and squamous tissues appears rigidlike with cells assuming highly isometric, low-$\langle p \rangle$ shapes, whereas cuboidal tissues appear floppylike with high-$\langle p \rangle$ cell shapes (Fig. 1).

Mapping to the 2D APE model—The results of our 3D simulations (Fig. 1) are indicative of a reentrant columnar-to-squamous rigidity transition. To assess their possible relation with the well-studied 2D APE model, we next project our model to 2D. In line with our vertex model, where $k_V = 100$, we assume $k_V \to \infty$ and thus $V_k = 1$ for all cells. By expressing cell geometry in terms of A, h, and P_k and accounting for the fixed-volume constraint, the single-cell energy becomes

$$W_k = A^{-2}[P_k - A(S_0 - 2A)]^2 - \frac{\gamma P_k}{2A}. \quad (3)$$

Since, at a given 3D cell aspect ratio ξ, the cell in-plane area is *a priori* imposed [Eq. (2)], A can be used to renormalize cell perimeters P_k as well as the energy. The single-cell energy, recast in terms of renormalized perimeter $p_k = P_k/\sqrt{A}$ and rescaled by A^{-1}, reads

$$w_k = (p_k - p_0)^2 + w_0, \quad (4)$$

where

$$p_0 = A^{1/2}\left(S_0 - 2A + \frac{\gamma}{4}\right) \quad (5)$$

is the preferred renormalized cell perimeter and $w_0 = \gamma A(16A - 8S_0 - \gamma)/16$. This mapping shows that, for any given in-plane cell area, set by in-plane strain, our $k_V \to \infty$-model maps exactly to a model describing a planar packing of unit-area polygons whose perimeters p_k tend toward p_0. In terms of p_k, w_0 can be seen merely as an energy offset.

Reentrant rigidity transition—This mapping allows us to simulate CST of 3D monolayers in 2D by minimizing the renormalized energy [Eq. (4)], while keeping all in-plane polygon areas fixed at 1. Because of the renormalization of cell sizes, the simulation-box size is kept fixed as well [Figs. 2(a) and 2(b)], but the in-plane strain and thus the change of the 3D cell aspect ratio ξ, associated with CST, is

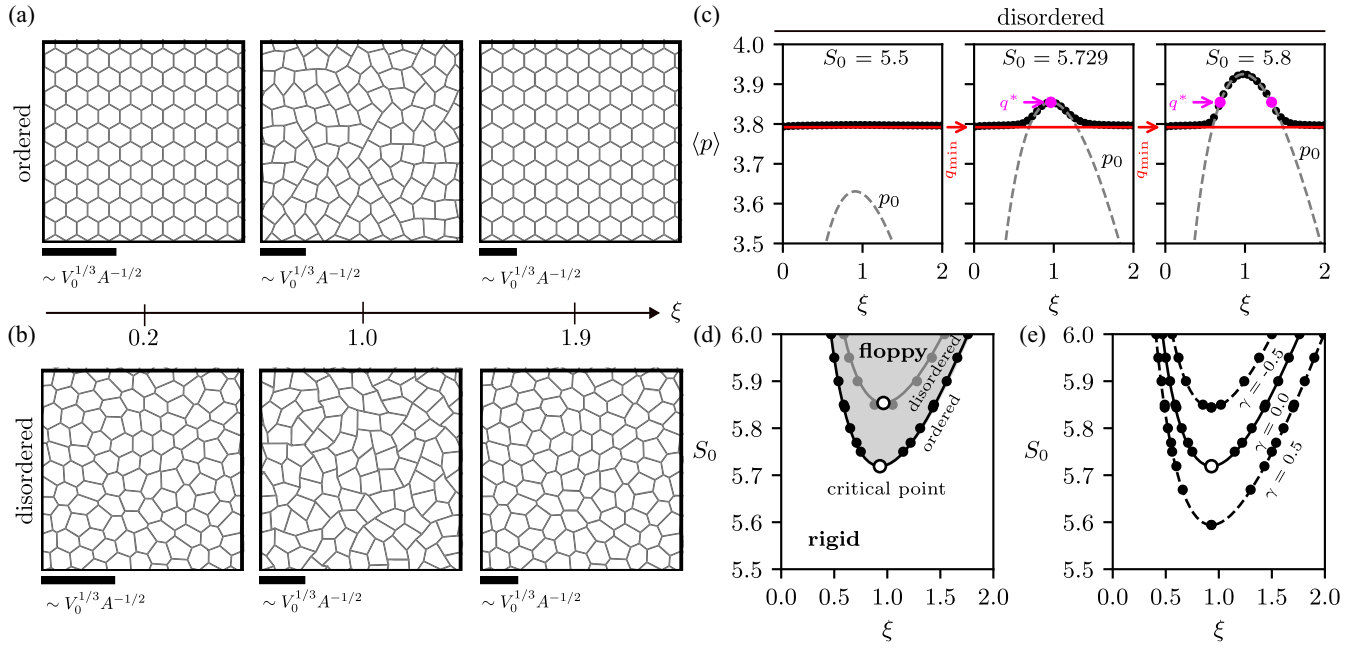

FIG. 2. (a),(b) Simulation snapshots of CST transition of ordered tissue for $S_0 = 5.75$ (a) and disordered tissue for $S_0 = 5.9$ (b). In both cases, $\gamma = 0.5$. Three-dimensional cell aspect ratio ξ increases from left to right. Scale bars indicate the absolute length scale $\sim V_0^{1/3}A^{-1/2}$. For clarity, $\sim$10% of cells are shown. (c) Average renormalized in-plane cell perimeter $\langle p \rangle$ versus ξ in disordered tissue with fraction of nonhexagons $d = 0.437$ for $S_0 = 5.5, 5.729$, and 5.8 (data points); $\gamma = 0.5$. Dashed gray curve and solid red line show p_0 [Eq. (5)] and $q_{\min}$, respectively. Tissues are compatible for $\langle p \rangle > q^*$; here q^* is the lowest p_0 value where all cells are compatible with the preferred shape. (d),(e) Rigidity diagram $S_0(\xi, \gamma)$ for $\gamma = 0$ (d) and for ordered tissues at $\gamma = -0.5, 0$, and 0.5 (e). Black and gray data points show simulation data and hollow circles indicate critical points. Phase boundaries [Eq. (6)] are shown by black and gray curves for ordered and disordered ($d = 0.437$) tissues, respectively (d). In simulations, tissues are classified as being compatible (floppy) when $|\langle p \rangle - p_0|$ is below a threshold. Because $|\langle p \rangle - p_0|$ decreases sharply at the transition, the classification is insensitive to the precise value of this threshold.

effectively simulated by quasistatically varying p_0 (and w_0) according to Eq. (5).

At a given cell aspect ratio ξ, the minimal possible renormalized energy $w = N_c w_0$ [Eq. (4)] is reached if all cells assume the preferred renormalized perimeter p_0. Such states are not possible if p_0 is too small, as every packing of equal-area polygons is characterized by a minimal attainable average cell-shape index $q_{\min}$. This minimal value depends on the packing's statistical properties: For a regular hexagonal packing, $q_{\min} = q_6 = 2^{3/2} \times 3^{1/4} \approx 3.722$, corresponding to the perimeter of unit-area regular hexagon, whereas in disordered packings, $q_{\min} > q_6$ [Supplemental Material, Figs. S2(a) and S2(b) [21]]. Tissues with $p_0 < q_{\min}$, therefore, necessarily describe geometrically incompatible, i.e., rigid, states. Plotting average renormalized in-plane cell perimeters $\langle p \rangle$ versus ξ shows that, for small enough S_0 values, these incompatible states appear along the whole range of 3D cell aspect ratios [Fig. 2(c), left and Supplemental Material, Fig. S2(d) [21]] and $\langle p \rangle$ in this regime is close to $q_{\min}$.

Geometrically compatible, i.e., floppy, states are present only for large enough S_0 values and appear for 3D cell aspect ratios close to unity, i.e., cuboidal tissues [Fig. 2(c), middle and right and Supplemental Material, Fig. S2(d) [21]], as observed in 3D simulations of CST (Fig. 1). Compatibility requires all cells assuming the preferred in-plane area (Supplemental Material, Fig. S3 [21]) and the preferred in-plane perimeter. Since renormalized in-plane cell perimeters of all cells in regular hexagonal packings can attain the minimal cell-shape index ($p_k = q_{\min} = q_6$), q_6 is at the same time the lowest p_0 value where the compatibility condition is met; we denote this value more generally by q^*. In contrast, in disordered tissues where perimeters are distributed, the lowest p_0 value where *all* cells are compatible with the preferred shape p_0 is $q^* > q_{\min}$. Like $q_{\min}$, q^* too depends on the degree of disorder [Supplemental Material, Figs. S2(b) and S2(c) [21]]. Thus, the general compatibility condition $p_k = p_0 = q^*$ yields the rigid-floppy boundary in the $S_0(\xi)$ diagram,

$$S_0(\xi) = \frac{q^* + 2\xi}{\xi^{1/3}} - \frac{\gamma}{4}. \tag{6}$$

This relation agrees perfectly with simulations [Figs. 2(d) and 2(e) and Supplemental Material, Figs. S2(e) and S2(f) [21]] and describes a reentrant rigidity transition, controlled by the in-plane isotropic strain through ξ.

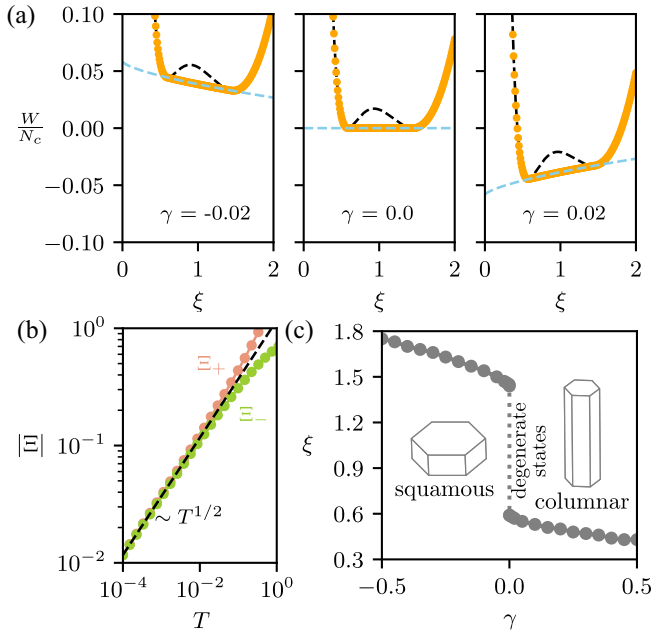

FIG. 3. (a) Total energy per cell, W/N_c, as a function of ξ for $\gamma = -0.02, 0$, and 0.02 (from left to right). Orange data points show numerical results, whereas dashed blue and black curves show $W_{\text{floppy}} = W(P = p_0\sqrt{A})$ and $W_{\text{rigid}} = W(P = q_6\sqrt{A})$, respectively. (b) The $T^{1/2}$-critical scaling of the order parameter $|\Xi|$. The two branches $\Xi_\pm$ denote the reentrant transition points $\xi_\pm - \xi^*$. (c) Equilibrium cell aspect ratio ξ versus lateral tension γ. (a),(c) A regular hexagonal packing with $S_0 = 5.85$ is considered.

The reentrant transition appears only for sufficiently high S_0: At $\xi^* = q^*/4$, where $\partial_\xi S_0 = 0$, the phase diagram features a critical point $S_0^* = 3 \times 2^{-1/3} q^{*2/3}$. For $S_0 < S_0^*$, there are no floppy states, regardless of the ξ value. For hexagonal cell packing, $\xi^* = 2^{-1/2} \times 3^{1/4} \approx 0.93$ and $S_0^* = 3^{7/6} \times 2^{2/3} \approx 5.719$.

An intuitive explanation for the observed reentrant rigidity transition is as follows: As the 3D cell aspect ratio deviates from a compatible cuboidal shape—either by becoming columnar or squamous—the total cell surface area increases. To maintain compatibility, this increase may be compensated by reducing the lateral surface area. Since for a given cell aspect ratio, cell height as well as apical and basal areas are fixed, the lateral surface area can only be reduced by shortening of the in-plane cell perimeter. However, when the average cell-shape index reaches q^*, this perimeter adjustment is no longer possible and tissue rigidifies.

Mean-field theory—To examine the emergence of the rigidity transition as S_0 crosses the critical point, we study the energy of a regular hexagonal cell arrangement, $F = W\left(P = q_6\sqrt{A}\right)$, recast in terms of the "order parameter" $\Xi = \xi - \xi^*$ and generalized "temperature" $T = S_0 - S_0^*$ (Supplemental Material, Sec. III [21]). We perform a fourth order Taylor expansion of F which for $\gamma = 0$ [Fig. 3(a), middle] reads

$$F \approx F_0 + a_2(T)\Xi^2 + a_3(T)\Xi^3 + a_4(T)\Xi^4. \tag{7}$$

Here, the quadratic coefficient scales linearly with T, as in the classical mean-field theory of the Ising model. The difference lies in the presence of the cubic term, whose presence at first glance suggests a discontinuous transition similar to the Landau–de Gennes theory of nematic-isotropic phase transition in liquid crystals. However, since a_3, like a_2, vanishes linearly with T, while the stabilizing quartic term approaches a positive constant (Supplemental Material, Sec. III [21]), the resulting critical behavior coincides—under the assumption of uniform cell height—with that of the classical Ising mean-field theory with the $T^{1/2}$-critical scaling of the order parameter, $|\Xi| = 3^{2/3}2^{-5/6}T^{1/2}$, describing the emergence of the reentrant transition points ξ_- and ξ_+ as T becomes positive [Fig. 3(b)].

For aspect ratios between ξ_- and ξ_+ [Fig. 3(a), middle], where cells are compatible with the preferred shape, the energy landscape, described by $W_{\text{floppy}} = W(P = p_0\sqrt{A})$, is flat, indicating that, in addition to the vanishing shear modulus, floppy states are also characterized by a zero in-plane bulk modulus, associated with isotropic in-plane deformations. Unlike in 2D, such deformations may occur at a constant energy, since (i) 3D cell volumes can be preserved under in-plane strain by adjusting cell height, whereas (ii) the change of the cell surface area, associated with varying cell aspect ratio, may be prevented by adjusting the in-plane polygon shape factor as discussed above. Notably, in 2D, similar energy-free isotropic deformations exist only in the trivial case, where cell-area elasticity is absent [14,19]. We note that resistance to cell-height fluctuations that may arise from the elasticity of cytoplasmic components [28] may lift this energy degeneracy (Supplemental Material, Fig. S4 [21]).

Expanding the analogy with the classical mean-field Ising model, we observe that the lateral tension γ contributes to the energy F [Eq. (7)] through an additional term $h\Xi$, where $h = 2^{7/6} \times 3^{-13/12}\gamma$ is a generalized external field. This field breaks the "up-down" symmetry, favoring squamous cells with $\xi = \xi_+$ when $\gamma < 0$ and columnar cells with $\xi = \xi_-$ when $\gamma > 0$ [Figs. 3(a) and 3(c)]. Near the critical point, the optimal cell aspect ratio $\xi = \xi^* + \chi\gamma$, with a generalized susceptibility $\chi \propto |T|^{-1}$, satisfying the universal ratio $\chi(T < 0)/\chi(T > 0) = 2$. At $T = 0$, the relation between ξ and γ is given by the critical "isotherm" $\gamma \propto -\Xi^3$. Overall, in our model with uniform cell heights, the critical scaling exponents are consistent with the Landau mean-field universality class (Supplemental Material, Sec. III [21]).

Discussion—Our results show that the rigidity of epithelia with VAE [Eq. (1)] may be tuned nonmonotonically by in-plane isotropic strain (Fig. 1), describing a reentrant

columnar-to-squamous rigidity transition, whereby tissues transition from rigid columnar to rigid squamous states, through intermediate floppy cuboidal states (Fig. 2). An additional constant lateral tension, distinguishing lateral from apical and basal sides, introduces a discontinuous CST with energy-degenerate states with zero in-plane bulk modulus, when lateral tension is absent (Fig. 3).

Interestingly, our 2D-projected model shows that varying 3D cell aspect ratio, i.e., by imposing in-plane isotropic strain, effectively corresponds to nonlinearly changing the effective in-plane preferred cell-shape index p_0 [Eq. (5)], which, in turn, controls the rigidity transition. This provides an alternative physical interpretation of p_0, which has been so far interpreted through a competition between cortical tension and adhesion strength [8,11].

The 2D APE model, which inherently does not describe cell height, counterintuitively and in contrast with the standard jamming [29] predicts tissue softening upon in-plane compression [18,19]. By accounting for the third dimension, our model changes this view. Indeed, compressing and dilating a monolayer away from a cuboidal state both lead to its rigidification (Fig. 1).

Our analysis also shows that the VAE monolayer model is a more direct 3D analog of the 2D APE model than the model in which apical cell sides, described by APE, are coupled to the basolateral cell domains under surface tension [17]. Indeed, while the apico- and basolateral coupling in the latter model prevents the rigidity transition altogether, our 3D VAE monolayer model preserves it and in the limit of incompressible cells even exactly maps to the 2D fixed-area APE model. We note that the rigidity transition persists even in a generalized version of our model, where cells are associated both with the preferred surface area and preferred apical perimeter (Supplemental Material, Fig. S5 [21]).

Finally, while the assumption that epithelial cells tend to preserve both their volumes and total surface areas is yet to be experimentally validated, this phenomenology may readily apply to studying synthetic planar packings of strongly adhering lipid vesicles, where the membrane's bending elasticity may be negligible and the mechanics may be well described by the VAE model [30].

Acknowledgments—We thank Tomaž Rejec, Silke Henkes, and members of her research group at the Lorentz Institute in Leiden for fruitful discussions, as well as Jan Rozman and Primož Ziherl for suggesting a generalization of our initial model. We acknowledge the financial support from the Slovenian Research and Innovation Agency (research projects J1-3009 and J1-60013, development funding pillar RSF-0106, and research core funding P1-0055). T. S. acknowledges IISER TVM for support.

Data availability—The data that support the findings of this article are openly available [31].

[1] A. Mongera, P. Rowghanian, H. J. Gustafson, E. Shelton, D. A. Kealhofer, E. K. Carn, F. Serwane, A. A. Lucio, J. Giammona, and O. Campàs, Nature (London) **561**, 401 (2018).
[2] R. J. Tetley, M. F. Staddon, D. Heller, A. Hoppe, S. Banerjee, and Y. Mao, Nat. Phys. **15**, 1195 (2019).
[3] J. H. Kim, A. F. Pegoraro, A. Das, S. A. Koehler, S. A. Ujwary, B. Lan, J. A. Mitchel, L. Atia, S. He, K. Wang, D. Bi, M. H. Zaman, J.-A. Park, J. P. Butler, K. H. Lee, J. R. Starr, and J. J. Fredberg, Biochem. Biophys. Res. Commun. **521**, 706 (2020).
[4] L. Atia, J. J. Fredberg, N. S. Gov, and A. F. Pegoraro, Cells Dev. **168**, 203727 (2021).
[5] E. Lawson-Keister and M. L. Manning, Curr. Opin. Cell Biol. **72**, 146 (2021).
[6] N. I. Petridou, B. Corominas-Murtra, C.-P. Heisenberg, and E. Hannezo, Cell **184**, 1914 (2021).
[7] E. Hannezo and C.-P. Heisenberg, Trends Cell Biol. **32**, 433 (2022).
[8] R. Farhadifar, J.-C. Röper, B. Aigouy, S. Eaton, and F. Jülicher, Curr. Biol. **17**, 2095 (2007).
[9] A. Hočevar and P. Ziherl, Phys. Rev. E **80**, 011904 (2009).
[10] D. B. Staple, R. Farhadifar, J. C. Röper, B. Aigouy, S. Eaton, and F. Jülicher, Eur. Phys. J. E **33**, 117 (2010).
[11] D. Bi, J. H. Lopez, J. M. Schwarz, and M. L. Manning, Nat. Phys. **11**, 1074 (2015).
[12] J.-A. Park *et al.*, Nat. Mater. **14**, 1040 (2015).
[13] M. Moshe, M. J. Bowick, and M. C. Marchetti, Phys. Rev. Lett. **120**, 268105 (2018).
[14] M. Merkel, K. Baumgarten, B. P. Tighe, and M. L. Manning, Proc. Natl. Acad. Sci. U.S.A. **116**, 6560 (2019).
[15] P. Sahu, J. Kang, G. Erdemci-Tandogan, and M. L. Manning, Soft Matter **16**, 1850 (2020).
[16] M. Merkel and M. L. Manning, New J. Phys. **20**, 022002 (2018).
[17] J. Rozman, M. Krajnc, and P. Ziherl, Phys. Rev. Lett. **133**, 168401 (2024).
[18] S. Tong, N. K. Singh, R. Sknepnek, and A. Košmrlj, PLoS Comput. Biol. **18**, 1 (2022).
[19] A. Hernandez, M. F. Staddon, M. Moshe, and M. C. Marchetti, Soft Matter **19**, 7744 (2023).
[20] The assumption of uniform cell height is reasonable because cells in a monolayer are tightly packed. If apical vertices were free to move in the z direction, the apical surface of the tissue would no longer remain generally flat. Nevertheless, the simplification of flat apical surface does not affect the main conclusions of our Letter.
[21] See Supplemental Material at http://link.aps.org/supplemental/10.1103/ky2j-5nwx for supporting derivations and figures, which includes Refs. [22–24].
[22] S. Curran, C. Strandkvist, J. Bathmann, M. de Gennes, A. Kabla, G. Salbreux, and B. Baum, Dev. Cell **43**, 480 (2017).
[23] M. Krajnc, Soft Matter **16**, 3209 (2020).
[24] M. Krajnc, T. Stern, and C. Zankoc, Phys. Rev. Lett. **127**, 198103 (2021).
[25] M. Krajnc, S. Dasgupta, P. Ziherl, and J. Prost, Phys. Rev. E **98**, 022409 (2018).

[26] L. Sui, S. Alt, M. Weigert, N. Dye, S. Eaton, F. Jug, E. W. Myers, F. Jülicher, G. Salbreux, and C. Dahmann, Nat. Commun. **9**, 4620 (2018).

[27] Apical and basal polygon collapses are known from other 3D monolayer models and are typically prevented by auxiliary energy terms that penalize vanishing polygon areas [26].

[28] E. Hannezo, J. Prost, and J.-F. Joanny, Proc. Natl. Acad. Sci. U.S.A. **111**, 27 (2014).

[29] A. J. Liu and S. R. Nagel, Nature (London) **396**, 21 (1998).

[30] A. Hočevar and P. Ziherl, Phys. Rev. E **83**, 041917 (2011).

[31] T. Sarkar and M. Krajnc, reentrant-rigidity-transition, 2026, https://gitlab.com/tanmoy_jsi/reentrant-rigidity-transition.